ACS APPLIED MATERIALS & INTERFACES

www.acsami.org

Research Article

Manipulation of Nitrogen-Heteroatom Configuration for Enhanced Charge-Storage Performance and Reliability of Nanoporous Carbon Electrodes

Sutarsis, Jagabandhu Patra, Ching-Yuan Su, Ju Li, Dominic Bresser, Stefano Passerini, and Jeng-Kuei Chang*

Cite This: *ACS Appl. Mater. Interfaces* 2020, 12, 32797−32805

Read Online

ACCESS | Metrics & More | Article Recommendations | Supporting Information

ABSTRACT: In this study, various nitrogen-containing functional groups, namely, pyridine (N-6), pyrrole (N-5), oxidized N (N−O), and quaternary N (N-Q), are created on activated carbon (AC) surface via melamine, ammonia, and nitric oxide doping methods. N-5 and N-6 groups markedly alter the specific surface area and pore size of AC. N−O is found to affect electrolyte wettability, and the N-Q content is closely associated with AC electronic conductivity. The nitrogen-containing groups do not contribute to pseudocapacitance in propylene carbonate and acetonitrile electrolytes. However, the nitric-oxide-treated carbon (AC-NO) exhibits the best high-rate charge−discharge performance among the investigated materials. The N-Q-enriched and N-5/N-6-depleted AC-NO most effectively suppresses the leakage current and gas evolution of supercapacitors. Online gas chromatography is used to analyze the gaseous species produced from AC electrodes. With an appropriate surface functionality on carbon, the cell voltage can be increased to ∼3 V, increasing the energy and power densities. The aging behavior of the carbon electrodes with and without nitrogen modification after being floated at 2.5 V and 70 °C for 3 days is investigated. An effective strategy for enhancing supercapacitor performance and reliability is proposed.

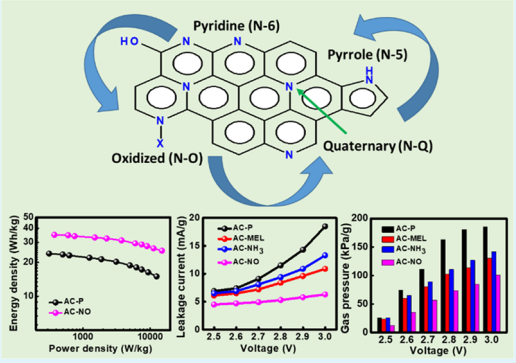

KEYWORDS: *electric double-layer capacitor, surface functionality, leakage current, gas evolution, cell aging*

1. INTRODUCTION

There is a high demand for an effective charge-storage device that has a high power density, a wide operating temperature range, excellent cycling stability, and high charge−discharge efficiency for application in regenerative braking systems and intermittent renewable energy storage.[1−4] Supercapacitors, especially electric double-layer capacitors (EDLCs), are appealing candidates for these applications. EDLCs store electric energy by forming an electrical double layer on the huge surface area of porous carbon; they have a high power density (up to $\sim 10^4$ W kg^{-1}), a long cycle life (up to millions of cycles), and high safety, and require no maintenance.[5,6] Recently, much effort has been devoted to increasing the energy density of EDLCs via improvements in electrode capacitance and cell voltage.[7,8] Power density, a major advantage of EDLCs over ordinary secondary batteries, is also crucial. An effective and facile material design method for increasing power density is thus highly desired.

The reliability of EDLCs, long overlooked, is important for practical applications. For instance, leakage current can lead to the self-discharge of EDLCs.[9,10] This not only results in energy loss but also generates heat during charging, complicating thermal management and accelerating EDLC fading.[11] Gassing during operation, which is associated with decomposition side reactions of the electrodes and the electrolyte, is another key issue.[11−13] Gas evolution can block the pores of the electrodes and separator and increase the EDLC internal resistance and pressure, leading to performance decay, cell rupture, and even safety risks.[14−16] In addition, the aging behavior of carbon electrodes is of great concern because long-term stability is expected for EDLCs.[14,17] In severe operation conditions or with prolonged charge/discharge cycles (especially at high voltages and elevated temperatures), unwanted faradic degradation reactions could occur, resulting in capacity decay and increased cell resistance.[3,4,18,19] Such reactions would shorten device lifetime. These reliability problems limit the applicability of EDLCs. Better electrode material design and control are required to overcome these problems.

Received: May 8, 2020
Accepted: June 19, 2020
Published: June 19, 2020

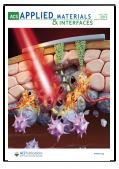

The doping of heteroatoms (such as N, B, P, O, and S) into carbon to improve the charge−discharge properties of EDLCs has attracted much attention.[20−22] Among the potential doping elements, nitrogen (N) is highly compelling.[20,23] In aqueous electrolyte, a N-doped carbon electrode showed improved electron transfer rate, wettability, and stability, and decreased equivalent series resistance.[24−27] Most importantly, the introduced pyridine and pyrrole groups strongly contributed to pseudocapacitive reactions,[25,27] increasing the electrode's specific capacitance. However, nonaqueous electrolytes are commonly used in practical applications because they allow much higher cell voltage (and thus energy and power densities) and longer cycle life than those obtained with aqueous electrolytes. It is noted that the working ions and solvation molecules in aqueous and nonaqueous electrolytes are different, and thus the optimal materials for these two types of electrolyte can be different. The behavior of N dopants in nonaqueous organic electrolytes is still ambiguous. Candelaria et al.[28] and Garcia et al.[29] found that pseudocapacitance arises from faradic reactions induced by lone electron pairs from N-containing groups interacting with electrolyte cations (i.e., $(C_2H_5)_4^+$). However, contradictory data were reported in other studies, which revealed that N-containing functional groups did not show any pseudocapacitive effect in nonaqueous electrolytes.[30−32] These inconsistent results may be associated with the fact that different doping methods create different types of N functionality (including pyridine, pyrrole, oxidized N, and quaternary N) that exhibit distinct electrochemical properties in the electrolyte. A more detailed and systematic investigation is thus needed to optimize surface functional group manipulation.

In the present study, melamine, ammonia, and nitric oxide doping methods are used to create various N-containing functional groups, namely, pyridine (N-6), pyrrole (N-5), oxidized N (N−O), and quaternary N (N-Q), on activated carbon (AC). The correlations between the type of N functional group and AC morphology, pore structures, carbon bonding characteristics, electronic conductivity, and contact angle toward a nonaqueous electrolyte are investigated. The charge−discharge performance, cycling stability, and electrochemical impedance spectroscopy (EIS) characteristics of various N-doped AC electrodes are systematically studied. Propylene carbonate (PC) and acetonitrile (ACN) with tetraethylammonium tetrafluoroborate ($TEABF_4$) salt are used as electrolytes. The effects of various N functionalities on the leakage current and gas evolution are examined for the first time. We also demonstrate that with an appropriate N functionality on the carbon electrode, the cell voltage can be effectively increased and the aging rate can be remarkably suppressed. Moreover, a thicker AC layer can be used without significantly sacrificing the specific power density.

2. EXPERIMENTAL SECTION

2.1. Material Preparation. AC powder ($D_{50} \sim 6\ \mu m$) supplied by the R & D department of China Steel Co., Ltd. was used as received. Three kinds of nitrogen doping procedure were used. (i) The AC was mixed with melamine in a mass ratio of 1:1 in ethanol solution and stirred for 24 h. The filtered powder was loaded into an alumina crucible and then heated (at 5 °C min^{-1}) in an airtight quartz tube under N_2 flow to 750 °C and held for 4 h. This sample is denoted as AC-MEL. (ii) The AC was heated under an NH_3/Ar mixed gas (50/50 cc min^{-1}) in an airtight quartz tube. The sample was heated at a rate of 5 °C min^{-1} to 750 °C and held for 4 h. This sample is denoted as AC-NH_3. (iii) The AC was treated with 3000 ppm NO, with He used as the carrier gas. The gas flow rate was 50 cc min^{-1}. The heating parameters were the same as those used for the NH_3 treatment. This sample is denoted as AC-NO. We intentionally controlled the precursor concentrations to make the N content levels of the three samples similar. For comparison, the as-received AC was heated under N_2 using the same temperature profile. This pristine sample is denoted as AC-P.

2.2. Material Characterization. X-ray photoelectron spectroscopy (XPS; Thermo Fisher Scientific ESCALAB Xi^+) was used to probe the surface chemistry of the AC samples. Monochromatic Al $K\alpha$ radiation was adopted as the X-ray source. The C 1s peak of graphitic carbon at 284.6 eV was used for binding energy calibration. To eliminate adsorbed contaminants, the AC samples were degassed under vacuum at 100 °C for 24 h before XPS measurements. The microstructures of the AC samples were examined using scanning electron microscopy (SEM; JEOL JSM-7800 F). A Raman spectrometer (UniRAM Micro Raman; λ = 532 nm) was used to analyze the carbon bonding characteristics. Nitrogen adsorption/desorption isotherms were acquired at −196 °C. The specific surface area and pore size were calculated using the quenched solid density functional theory model, and the pore geometry was assumed to be slit-shaped. Contact angle measurements were conducted using the static sessile drop method. A digital goniometer was used to record the contact angle after 0.2 mL of 1 M $TEABF_4$/PC electrolyte had been dropped onto the AC electrode.

2.3. Electrode Preparation and Electrochemical Property and Reliability Measurements. An electrode slurry was prepared by mixing 91 wt % AC powder, 2.5 wt % carbon black, 5 wt % styrene-butadiene rubber, and 1.5 wt % sodium carboxymethyl cellulose in deionized water. The slurry was pasted onto etched Al foil and vacuum-dried at 90 °C for 6 h. The final thickness of the coating layer was ∼35 μm with an AC loading amount of ∼1.4 mg cm^{-2}. The obtained electrode was then punched to match the required dimensions of a CR2032 coin cell. Two symmetrical electrodes divided by a cellulose separator were assembled in a coin cell. The electrolyte was composed of 1 M $TEABF_4$ salt (99 wt %, Alfa Aesar) in PC (99.7 wt %, Sigma-Aldrich) or ACN (99.5 wt %, J.T. Baker) solvent. The coin cell assembly was conducted in an argon-filled glovebox (Innovation Technology Co. Ltd), where both the moisture and oxygen content levels were below 0.3 ppm.

Galvanostatic charge−discharge tests were performed using a Solartron 1470E potentiostat with various applied current densities. The leakage current was measured after the cells were held at the set voltage for 2 h. The gas evolution of the AC electrodes was evaluated using a custom-made electrochemical cell equipped with a pressure gauge, which has an accuracy of 0.5 kPa. The symmetrical cell was galvanostatically charged to various voltages, and the pressure increase was recorded after 6 h. The produced gaseous species were further analyzed using online gas chromatography (GC; Shimadzu GC-2010 Plus). Helium was used as the carrier gas. Aging tests were performed by holding the cells at 2.5 V and 70 °C for 3 days. EIS was employed to characterize the impedance properties before and after cell aging. The frequency range and voltage amplitude, regulated using a BioLogic VSP-300 potentiostat, were 10^5−10^{-2} Hz and 10 mV, respectively. A postmortem electrode morphology examination was carried out with SEM.

3. RESULTS AND DISCUSSION

3.1. Surface Functionality. To evaluate the surface chemical compositions of the AC samples, XPS analyses were performed. The obtained survey scan data are shown in Figure 1a. Except for AC-P, which did not contain any N, the samples exhibited clear C 1s, O 1s, and N 1s signals. No other elements were detected, indicating high purity. The N concentrations of AC-MEL, AC-NH_3, and AC-NO were 3.5, 3.2, and 3.3 atom %, respectively, indicating that the N doping procedure did not significantly affect the N content.

https://dx.doi.org/10.1021/acsami.0c08440
ACS Appl. Mater. Interfaces 2020, 12, 32797−32805

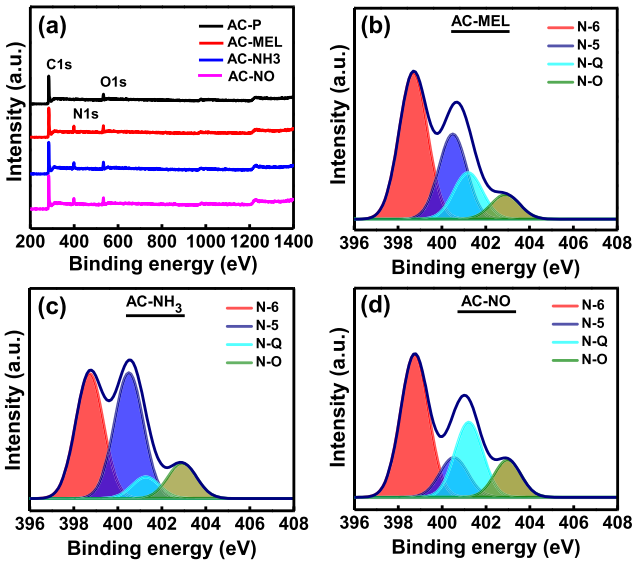

Figure 1. XPS (a) survey scan and (b–d) N 1s narrow-scan spectra of various AC samples.

Figure 1b–d shows that the types of N functional group on the AC samples depend on the N doping procedure. The N 1s binding energies of 398.7, 400.5, 401.3, and 402.9 eV can be assigned to N-6, N-5, N-Q, and N–O, respectively.[25] Among the samples, as shown in Table 1, AC-NH_3 had the most (N-5 + N-6) and the least N-Q. In contrast, AC-NO had the least (N-5 + N-6) and the most N-Q. AC-MEL had moderate concentrations of (N-5 + N-6) and N-Q. Ammonia gas and melamine preferably react with the surface oxygen-containing functional groups on AC, forming various N functional groups.[33−35] Because the replacement reactions mainly occur at the AC surface, the formation of N-5 and N-6 is preferential.[35,36] The reaction of the NO gas toward carbonaceous materials can be expressed as[37]

$$C_n + NO \rightarrow C_{n-1}N + CO$$

This suggests that N could substitute bulk carbon atoms, leading to the preferential formation of N-Q. It is noted that the oxidizing atmosphere of NO gas is probably responsible for the higher N–O content of AC-NO compared to that in the other samples. The effects of various N functionalities on the material properties and electrochemical performance are investigated later in this work. The narrow-scan C 1s XPS data for AC-P, AC-MEL, AC-NH_3, and AC-NO are shown in Figure S1. The spectra can be deconvoluted into five peaks, namely, those corresponding to C–C, C–N/C–H, C–OH, C═O, and COOH bonds.[11,14,38] As shown in Table S1, N doping increased the C–N bond fraction and reduced the concentrations of various oxygen-containing functional groups that formed during the chemical activation and rinsing processes of the AC synthesis. The content levels of the C–OH, C═O, and COOH groups on the three types of N-doped AC were similar. The O concentration of AC-P was 6.0 atom %, whereas those of the N-doped ACs were reduced to be approximately 3.9 atom %.

Table 1. Ratios of Various N Functional Groups for AC-MEL, AC-NH_3, and AC-NO Samples Calculated from XPS N 1s Spectra

	AC-MEL	AC-NH_3	AC-NO
pyridine (%)	41.2	42.0	40.0
pyrrole (%)	32.2	40.2	17.8
quaternary N (%)	19.6	7.0	29.1
oxidized N (%)	7.0	10.8	13.1

3.2. Physical Properties. Figure 2a shows the SEM images of the AC samples. N doping, regardless of the applied method, did not significantly affect the AC morphology. However, it slightly increased the Raman D-to-G band ratio. As shown in Figure 2b, the D band (at ~1350 cm^{-1}) and G band (at ~1590 cm^{-1}) can be clearly recognized in the Raman spectra. The former is associated with imperfect sp^2 carbon bonding, whereas the latter results from the Raman-allowed phonon vibration of well-ordered graphite.[39,40] The D-to-G band intensity ratios (I_D/I_G) for AC-P, AC-MEL, AC-NH_3, and AC-NO are 0.960, 1.011, 1.013, and 1.038, respectively. The nitrogen doping induced heterogeneous sites among the carbon lattice, marginally decreasing the degree of graphitization.

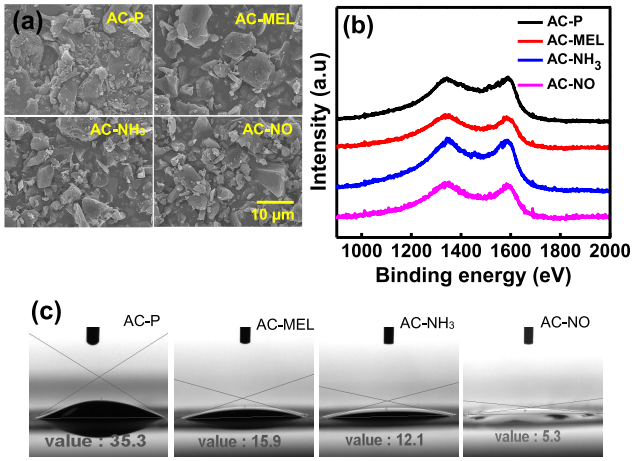

Figure 2. (a) SEM images, (b) Raman spectra, and (c) contact angle images of various AC samples.

The specific surface area and pore size distribution of the pristine and N-doped AC samples are shown in Table 2. AC-P had a specific surface area of 2102 $m^2\ g^{-1}$, with 728, 1188, and 186 $m^2\ g^{-1}$ contributed from micropores, mesopores, and macropores, respectively. The melamine treatment decreased the specific surface area to 1818 $m^2\ g^{-1}$ and altered the pore structure. The micropore and mesopore surface areas were reduced, whereas the macropore area was considerably increased (compared to those for AC-P). The surface N can affect the pyrolysis behavior of the underlying carbon at a high temperature, leading to pore structure variation.[28] A previous study also revealed that melamine tends to decrease carbon porosity and develop relatively large pores.[41] Table 2 also reveals that the NH_3 treatment significantly collapsed the mesopores but increased the macropore surface area. The micropore area developed due to the etching effects of NH_3 toward carbon.[33,42] Because a high percentage of the N functional groups (i.e., N-5 and N-6) is situated on the carbon edge of AC-MEL and AC-NH_3, the surface area and pore structure are prone to be altered. In contrast, the NO treatment did not significantly affect the AC specific surface area and pore size distribution, with 738, 1196, and 195 $m^2\ g^{-1}$ for micropores, mesopores, and macropores, respectively. This

https://dx.doi.org/10.1021/acsami.0c08440
ACS Appl. Mater. Interfaces 2020, 12, 32797−32805

Table 2. Specific Surface Areas of Micropores, Mesopores, and Macropores and Their Ratios for Various AC Samples Calculated from N_2 Adsorption/Desorption Isotherms

	AC-P		AC-MEL		AC-NH_3		AC-NO	
	area (m^2 g^{-1})	ratio (%)	area (m^2 g^{-1})	ratio (%)	area (m^2 g^{-1})	ratio (%)	area (m^2 g^{-1})	ratio (%)
micropores	728	35	673	37	878	46	738	35
mesopores	1188	56	714	39	560	29	1196	56
macropores	186	9	431	24	491	25	195	9
total	2102	100	1818	100	1929	100	2129	100

Table 3. Electronic Conductivity (σ), Interfacial Contact Resistance (R_{inter}), and Apparent Diffusion Coefficient (D_a) Values for Various AC Samples

	AC-P	AC-MEL	AC-NH_3	AC-NO
σ (S m^{-1})	9.3	17.7	12.1	19.7
R_{inter} (Ω)	3.3	1.8	2.1	1.6
D_a (cm^2 s^{-1})	1.56×10^{-7}	4.32×10^{-7}	1.02×10^{-7}	7.86×10^{-7}

indicates that the NO doping method best preserves the AC pore structure.

The electronic conductivity of the AC samples was measured using a four-point-probe method.[43] The AC-P, AC-MEL, AC-NH_3, and AC-NO slurries were coated onto plastic substrates, which provided no electronic conduction. Table 3 shows that all N-doped AC samples had considerably higher conductivity than AC-P. Of note, the conductivity values increased with increasing N-Q concentration in the AC samples. The graphitic center N donates a free electron within the sp^2 carbon structure,[44,45] effectively increasing the electronic conductivity of the N-doped AC samples. It has been reported that the carbon material containing N-Q functional groups has a smaller energy gap between the highest occupied molecular orbital and the lowest unoccupied molecular orbital compared to the carbons with other N-containing groups.[46] This explains the strong correlation between the electronic conductivity values (Table 3) and the N-Q content in our AC samples.

Figure 2c shows the wettability of 1 M $TEABF_4$/PC electrolyte toward the AC samples. The contact angles for the AC-P, AC-MEL, AC-NH_3, and AC-NO electrodes are 35, 16, 12, and 5°, respectively. It is noted that the electrode morphology and porosity also affect the contact angle.[47,48] However, these factors have similar effects for AC-P and AC-NO. These results imply that N functionality played a role in wettability improvement. A comparison of the contact angle data and the N group concentrations in Table 1 suggests that the N−O amount could be an important factor for the electrolyte wettability. Although the C−OH, C═O, and COOH groups also increase the wettability, their effects are minor because the AC-P showed the highest contact angle.

3.3. Electrochemical Charge−Discharge Performance. To evaluate the electrochemical characteristics of the AC electrodes, galvanostatic charge−discharge measurements were performed. As shown in Figure 3a, the charge−discharge curves for all of the electrodes have a nearly triangular shape, indicating ideal capacitive behavior in the $TEABF_4$/PC electrolyte. The overlapping curves at 0.5 A g^{-1} reveal that the specific capacitances are almost identical, as listed in Table 4. The results confirm that the introduced N groups did not show pseudocapacitive effects in the nonaqueous electrolyte. This is also supported by the cyclic voltammetry (CV) data shown in Figure S2, which shows an ideally rectangular shape for both AC-P and AC-NO electrodes. However, when the

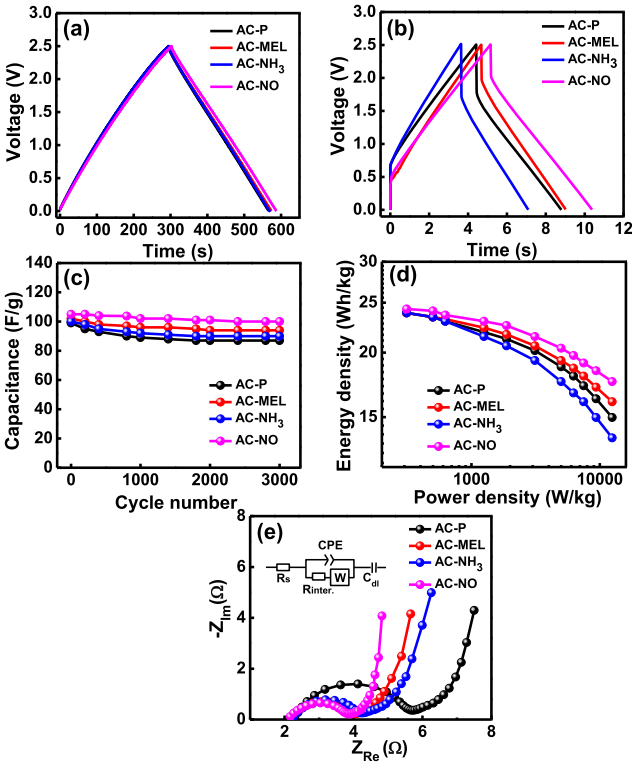

Figure 3. Galvanostatic charge−discharge curves measured at (a) 0.5 Ag^{-1} and (b) 20 Ag^{-1}. (c) Cyclic stability at 5 A g^{-1}, (d) Ragone plots and (e) EIS spectra of various AC cells.

Table 4. Specific Capacitances (F g^{-1}) and Capacitance Retention Ratios at 20 A g^{-1} (Compared to That at 0.5 A g^{-1}, $C_{20}/C_{0.5}$) of Various Electrodes Measured in 1 M $TEABF_4$/PC Electrolyte

current density (A g^{-1})	AC-P	AC-MEL	AC-NH_3	AC-NO
0.5	110	110	110	112
10	83	86	77	91
20	69	74	63	81
$C_{20}/C_{0.5}$ (%)	63	67	57	72

specific current was increased to 20 A g^{-1}, as shown in Figure 3b, the electrodes exhibited different charge−discharge properties. Table 4 shows that the specific capacitances of AC-P, AC-MEL, AC-NH_3, and AC-NO at 20 A g^{-1} were 69,

https://dx.doi.org/10.1021/acsami.0c08440
ACS Appl. Mater. Interfaces 2020, 12, 32797−32805

74, 63, and 81 F g^{-1}, respectively. Among the electrodes, AC-NH_3 showed lower high-rate performance (even worse than that of AC-P), probably because of its lower portion of mesopores, which are beneficial for electrolyte ion transport.[49,50] AC-MEL had markedly better rate capability than AC-NH_3. Besides the greater portion of mesopores, the higher percentage of N-Q (and thus higher conductivity) in AC-MEL is responsible for the improved performance. AC-NO, with even more mesopores and higher N-Q content, was found to be optimal. As shown in Figure 3b, the AC-NO electrode had the smallest IR drop and the longest charge−discharge duration, resulting in the highest specific capacitance. Figure 3c shows that the AC-NO electrode had the best cycling stability of all of the tested electrodes. The Ragone plots in Figure 3d indicate that N doping is unlikely to lead to pseudocapacitance but does affect the high-power capability of cells with an organic electrolyte. The data also reveal that the N doping method matters.

Figure 3e shows the EIS spectra of various cells. The Nyquist plots are characterized by a semicircle (associated with interfacial contact resistance) at high frequency, a nearly 45° sloping line (associated with ion diffusion impedance within AC pores) at intermediate frequency, and a quasi-vertical line (associated with capacitive behavior) at low frequency.[40,51,52] The equivalent circuit used to fit the EIS data is shown in the inset. As shown in Table 3, the interfacial contact resistance (R_{inter}) values of the AC-P, AC-MEL, AC-NH_3, and AC-NO cells were 3.3, 1.8, 2.1, and 1.6 Ω, respectively. This trend is consistent with that of the N-Q content ratio. A higher N-Q concentration led to a lower R_{inter} value. The apparent diffusion coefficients (D_a) can be calculated from the sloping line at intermediate frequency of the Nyquist plots.[53] As summarized in Table 3, the D_a values for the AC-P, AC-MEL, AC-NH_3, and AC-NO cells were 1.56×10^{-7}, 4.32×10^{-7}, 1.02×10^{-7}, and 7.86×10^{-7} cm^2 s^{-1}, respectively. The highest D_a was obtained for AC-NO; this can be attributed to the preservation of the surface area and pore structure and to the relatively high content of N−O groups, which increased the wettability and thus electrolyte ion transport within the AC pores.

The electrochemical properties of the AC-P and AC-NO electrodes in the other commonly used EDLC electrolyte $TEABF_4$/ACN were also compared. The obtained data are shown in Figure S3. Improved rate capability and cycling stability of the latter electrode were confirmed, indicating that the NO treatment is promising also for the acetonitrile-based electrolyte.

3.4. EDLC Reliability Study. The leakage current was measured after the cells were held at a constant voltage for 2 h. The data obtained are shown in Figure 4a. For an ideal capacitor, there should be no leakage current. Leakage current can be attributed to reversible and irreversible side reactions of the electrodes with the electrolyte. As shown, the leakage current of the AC-P cell dramatically increased after 2.7 V and was notably higher than those of the N-doped AC cells, which is due to the prominent decomposition of the oxygen-containing functional groups.[11,54,55] It is noted that the measured leakage current decreases in the order of AC-NH_3 > AC-MEL > AC-NO. The negatively charged N-5 and N-6, due to their nucleophilic nature, can facilitate PC ring opening,[56] leading to a side reaction current. In contrast, the positively charged N-Q reduces the possibility of nucleophilic attack, thus explaining the optimal stability of the AC-NO cell.

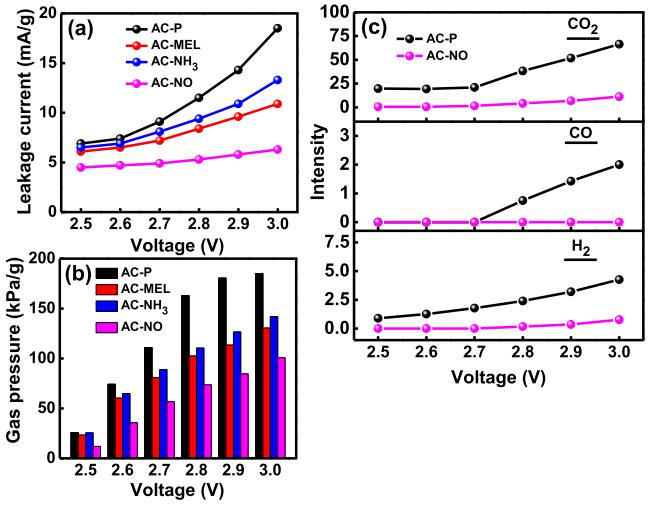

Figure 4. (a) Leakage current and (b) gas evolution data of various AC cells measured at different voltages. (c) Online GC data of CO_2, CO, and H_2 produced at different voltages.

Figure 4b shows the gas pressure of the cells, which were held at the set voltage for 6 h. The generated gas can deteriorate capacitor performance (similar to the Leidenfrost effect in boiling) and even lead to mechanical damage such as rupture and leakage of the cells. As shown, the gas pressure increases with the applied voltage. However, the cells containing the N-doped AC electrodes showed reduced gassing. Regardless of the voltage, the gas evolution tendency is AC-P > AC-NH_3 > AC-MEL > AC-NO, which is in line with that of the leakage current. These results confirm that the N-Q group most effectively suppresses unwanted faradic side reactions.

The gaseous products formed in the AC-P and AC-NO cells were analyzed using an online GC analyzer; the results are shown in Figure 4c. The AC-P cell generated remarkably more H_2, CO, and CO_2 gases than the AC-NO cell did, especially when the voltage was above 2.7 V. Besides the electrolyte decomposition, the oxygen-containing groups (such as carboxyl, phenol, ketone, and lactone) on AC-P can be easily oxidized, producing CO and CO_2.[14,57,58] These oxygen-containing groups are hydrophilic and tend to adsorb water molecules on the carbon surface.[46,47] At the negative electrode, electrolysis of the adsorbed water generates H_2 and OH^-, which further reacts with PC to form more CO and CO_2.[57,58] The NO treatment was confirmed to effectively reduce the above gassing reactions.

A promising strategy for improving the energy density and power density of a supercapacitor is to increase the cell voltage. To evaluate the effect of N doping on the cell voltage, galvanostatic charge−discharge tests were performed with various voltage windows. Figure 5a,b shows the specific capacitance and high-rate retention of the AC-P and AC-NO cells, respectively, measured in a voltage range of 2.5−3.50 V. The AC-P cell was stable up to 2.75 V but showed a significant performance decay when the voltage exceeded this limit. In contrast, for the AC-NO cell, degradation started at 3.25 V (the detailed capacitance and high-rate retention values are shown in Table S2). Figure 5c shows that the capacitance retention values after 3000 charge−discharge cycles for the AC-P cells operated within 2.5 and 3.0 V (@5 A g^{-1}) were 88 and 70%, respectively. The AC-NO cells showed 96%

https://dx.doi.org/10.1021/acsami.0c08440
ACS Appl. Mater. Interfaces 2020, 12, 32797−32805

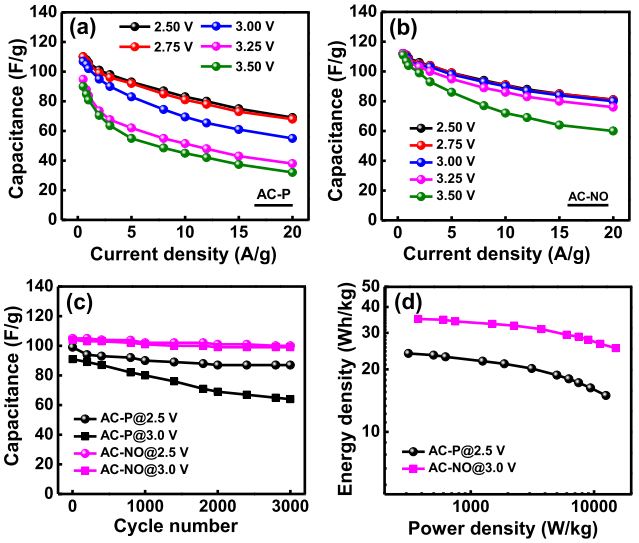

Figure 5. Specific capacitances at various rates for (a) AC-P and (b) AC-NO electrodes measured at different voltages. (c) Cycling stability and (d) Ragone plots of AC-P and AC-NO cells measured at different voltages.

capacitance retention for both operation voltages after the same number of cycles, indicating high reliability for 3 V applications. The N-doped AC has a lower oxygen-containing group concentration and shows suppression of electrolyte decomposition side reactions. As a result, an increased operation voltage can be realized. Figure 5d compares the Ragone plots of the AC-P cell operated within 2.5 V and the AC-NO cell operated within 3.0 V. The specific energy of the former cell was 23.9 Wh kg^{-1} at a specific power of 0.3 kW kg^{-1}, but it decreased to 14.9 Wh kg^{-1} at 12.5 kW kg^{-1}. For the latter cell, the specific energy values increased to 35.0 Wh kg^{-1} (at 0.4 kW kg^{-1}) and 25.3 Wh kg^{-1} (at 15.0 kW kg^{-1}), respectively.

In practical applications, a thick AC layer is preferred to reduce the inactive current collector ratio within a cell. To investigate the influence of N doping on the electrode thickness effects, AC-P and AC-NO layers with two thicknesses (35 and 100 μm) were prepared and their charge−discharge properties were examined. As shown in Figure S4a,b, at 0.5 A g^{-1}, all of the cells, regardless of the electrode composition and thickness, exhibited similar charge−discharge behavior and capacitances. However, at a high current density, the capacitance of the thick AC-P (100 μm) electrode significantly decreased. The capacitance retention ratio at 20 A g^{-1} (compared to that at 0.5 A g^{-1}, $C_{20}/C_{0.5}$) was 31%, which is much lower than that (63%) for the thin AC-P (35 μm) electrode (see Table 5). For the thick and thin AC-NO electrodes, the $C_{20}/C_{0.5}$ ratios were 56 and 72%, respectively. Figure S4c,d shows that at high current densities the IR drop for the 100 μm AC-NO cell was smaller than that for the 100 μm AC-P cell. The higher electronic conductivity and higher D_a value allowed the AC-NO electrode to be thicker without significant deterioration of the specific capacitance.

Figure 6a shows the variations of energy versus power performance of the AC-P and AC-NO cells after being floated at 2.50 V and 70 °C for 3 days. The former cell showed dramatic performance fading, especially in terms of power capability, whereas the latter cell exhibited improved stability.

Table 5. Specific Capacitances (F g^{-1}) and Capacitance Retention Ratios of AC-P and AC-NO Electrodes with Various Thicknesses Measured in 1 M $TEABF_4$/PC Electrolyte

	AC-P		AC-NO	
current density (A g^{-1})	35 μm	100 μm	35 μm	100 μm
0.5	110	110	112	112
10	83	73	91	82
20	69	34	81	63
$C_{20}/C_{0.5}$ (%)	63	31	72	56

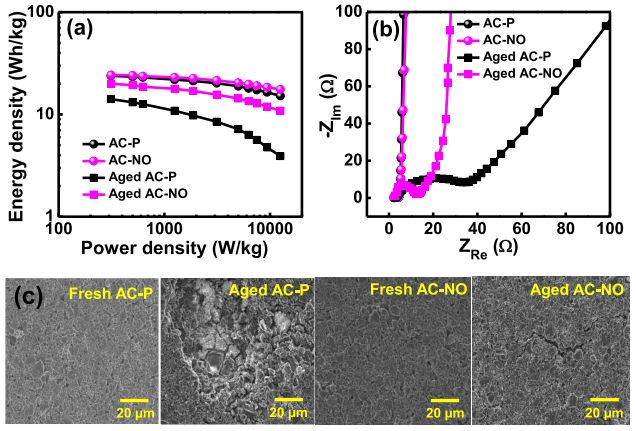

Figure 6. (a) Ragone plots and (b) EIS spectra of AC-P and AC-NO cells before and after being floated at 2.50 V and 70 °C for 3 days. (c) SEM images of fresh and aged electrodes.

Figure 6b shows the EIS data for the AC-P and AC-NO cells before and after aging. The R_{inter} and D_a values are summarized in Table S3. The electrode and electrolyte decomposition products that accumulated between AC particles (increasing R_{inter}) and within the AC pores (decreasing D_a) contributed to the cell performance decay. As shown in Figure 6b and Table S3, both R_{inter} and D_a deteriorations of the AC electrode were effectively suppressed after NO treatment. The relatively large degradation of the AC-P electrode upon aging was confirmed by SEM, as shown in Figure 6c. The interparticle cracking and structural collapse of the aged AC-P electrode are mainly ascribed to gas evolution, which physically destroyed the electrode.[11,14,59] Decomposition products generated from undesired faradic side reactions were observed. In addition, some corrosion damage was recognized. The adsorbed water molecules on the hydrophilic surface of AC-P are speculated to react with BF_4^- and then produce HF, which can corrode the active material and current collector.[60,61] These structural degradation issues are substantially mitigated for the AC-NO electrode.

4. CONCLUSIONS

The N doping of AC did not contribute to additional pseudocapacitance. However, the nitrogen-containing functional groups greatly affected the material properties and EDLC performance. The formation of N-5 and N-6 groups decreased the specific surface area and mesopore fraction of AC. The N-Q content was closely related to the AC electronic conductivity, while the N−O content affected the electrolyte wetting. The AC-NO electrode, having high N-Q and N−O contents, showed the best high-rate charge−discharge performance. The magnitude of leakage current and gas evolution of

https://dx.doi.org/10.1021/acsami.0c08440
ACS Appl. Mater. Interfaces 2020, 12, 32797−32805

the AC electrode depended on the type of N group, with N-Q being more favorable than N-5 and N-6 to suppress unwanted faradic side reactions. Online GC confirmed that the CO, CO_2, and H_2 gases produced via the electrolyte, electrode functional groups, and adsorbed water decomposition were considerably lower for the AC-NO cell than for the AC-P cell. Employing the AC-NO electrodes can effectively increase the cell voltage up to 3 V, increasing the specific energy and power of the cell. AC-NO also allowed for higher electrode thickness (due to higher electronic conductivity and D_a than those of AC-P), which is beneficial for practical applications. It was also found that the electrode aging rate, in terms of capacitance, R_{inter}, D_a, and structural degradation, can be adequately retarded with the NO treatment. The proposed N functionality design strategy could be applicable to other carbon-based electrode materials to enhance their electrochemical properties and reliability for energy storage applications.

■ ASSOCIATED CONTENT

Supporting Information

The Supporting Information is available free of charge at https://pubs.acs.org/doi/10.1021/acsami.0c08440.

Ratios of various functional groups for AC-P, AC-MEL, AC-NH_3, and AC-NO samples calculated from XPS; specific capacitances (F g^{-1}) at various rates for AC-P and AC-NO electrodes measured at different voltages in 1 M $TEABF_4$/PC electrolyte; interfacial contact resistance (R_{inter}) and apparent diffusion coefficient (D_a) values of AC-P and AC-NO cells before and after being floated at 2.50 V and 70 °C for 3 days; XPS C 1s spectra of AC-P, AC-MEL, AC-NH_3, and AC-NO samples; CV curves of AC-P and AC-NO cells measured at 5 mV s^{-1}; specific capacitances of AC-P and AC-NO electrodes measured at various rates in 1 M $TEABF_4$/ACN electrolyte; cycling stability of AC-P and AC-NO cells measured at 5 A g^{-1} in 1 M $TEABF_4$/ACN electrolyte; Galvanostatic charge−discharge curves measured at 0.5, 10, and 20 A g^{-1} with various electrode thicknesses; and specific capacitances of electrodes with various AC types and thicknesses (PDF)

■ AUTHOR INFORMATION

Corresponding Author

Jeng-Kuei Chang − *Institute of Materials Science and Engineering, National Central University, Taoyuan 32001, Taiwan; Hierarchical Green-Energy Materials (Hi-GEM) Research Center, National Cheng Kung University, Tainan 70101, Taiwan; Department of Materials Science and Engineering, National Chiao Tung University, Hsinchu 30010, Taiwan;* orcid.org/0000-0002-8359-5817; Phone: +886-3-5712121; Email: jkchang@nctu.edu.tw

Authors

Sutarsis − *Institute of Materials Science and Engineering, National Central University, Taoyuan 32001, Taiwan*

Jagabandhu Patra − *Hierarchical Green-Energy Materials (Hi-GEM) Research Center, National Cheng Kung University, Tainan 70101, Taiwan; Department of Materials Science and Engineering, National Chiao Tung University, Hsinchu 30010, Taiwan;* orcid.org/0000-0002-9783-3097

Ching-Yuan Su − *Department of Mechanical Engineering and Graduate Institute of Energy Engineering, National Central University, Taoyuan 32001, Taiwan;* orcid.org/0000-0001-9295-7587

Ju Li − *Department of Nuclear Science and Engineering and Department of Materials Science and Engineering, Massachusetts Institute of Technology, Cambridge, Massachusetts 02139, United States;* orcid.org/0000-0002-7841-8058

Dominic Bresser − *Helmholtz Institute Ulm (HIU), D-89081 Ulm, Germany; Karlsruhe Institute of Technology (KIT), 76021 Karlsruhe, Germany;* orcid.org/0000-0001-6429-6048

Stefano Passerini − *Helmholtz Institute Ulm (HIU), D-89081 Ulm, Germany; Karlsruhe Institute of Technology (KIT), 76021 Karlsruhe, Germany;* orcid.org/0000-0002-6606-5304

Complete contact information is available at: https://pubs.acs.org/10.1021/acsami.0c08440

Notes

The authors declare no competing financial interest.

■ ACKNOWLEDGMENTS

The financial support provided for this work by the Ministry of Science and Technology (MOST) of Taiwan, the German Federal Ministry of Education and Research (BMBF; 03XP0138C), and the China Steel Corporation of Taiwan is gratefully appreciated.

■ REFERENCES

(1) González, A.; Goikolea, E.; Barrena, J. A.; Mysyk, R. Review on Supercapacitors: Technologies and Materials. *Renewable Sustainable Energy Rev.* **2016**, *58*, 1189−1206.

(2) Miller, J. R.; Simon, P. Electrochemical Capacitors for Energy Management. *Science* **2008**, *321*, 651−652.

(3) Kötz, R.; Hahn, M.; Gallay, R. Temperature Behavior and Impedance Fundamentals of Supercapacitors. *J. Power Sources* **2006**, *154*, 550−555.

(4) Bohlen, O.; Kowal, J.; Sauer, D. U. Ageing Behaviour of Electrochemical Double Layer Capacitors: Part I. Experimental Study and Ageing Model. *J. Power Sources* **2007**, *172*, 468−475.

(5) Simon, P.; Gogotsi, Y. Materials for Electrochemical Capacitors. *Nat. Mater.* **2008**, *7*, 845−854.

(6) Wang, Q.; Yan, J.; Fan, Z. Carbon Materials for High Volumetric Performance Supercapacitors: Design, Progress, Challenges and Opportunities. *Energy Environ. Sci.* **2016**, *9*, 729−762.

(7) Wang, G.; Zhang, L.; Zhang, J. A Review of Electrode Materials for Electrochemical supercapacitors. *Chem. Soc. Rev.* **2012**, *41*, 797−828.

(8) Zhang, L. L.; Zhao, X. S. Carbon-Based Materials as Supercapacitor Electrodes. *Chem. Soc. Rev.* **2009**, *38*, 2520−2531.

(9) Conway, B. E.; Pell, W. G.; Liu, T. C. Diagnostic Analyses for Mechanisms of Self-Discharge of Electrochemical Capacitors and Batteries. *J. Power Sources* **1997**, *65*, 53−59.

(10) Ike, I. S.; Sigalas, I.; Iyuke, S. Understanding Performance Limitation and Suppression of Leakage Current or Self-Discharge in Electrochemical Capacitors: A Review. *Phys. Chem. Chem. Phys.* **2016**, *18*, 661−680.

(11) Nguyen, Q. D.; Wu, Y. H.; Wu, T. Y.; Deng, M. J.; Yang, C. H.; Chang, J. K. Gravimetric/volumetric Capacitances, Leakage Current, and Gas Evolution of Activated Carbon Supercapacitors. *Electrochim. Acta* **2016**, *222*, 1153−1159.

(12) Kötz, R.; Hahn, M.; Ruch, P.; Gallay, R. Comparison of Pressure Evolution in Supercapacitor Devices using Different Aprotic Solvents. *Electrochem. Commun.* **2008**, *10*, 359−362.

(13) Kim, J.; Kim, E.; Lee, U.; Lee, I.; Han, S.; Son, H.; Yoon, S. Nondisruptive in-situ Raman Analysis for Gas Evolution in

Commercial Supercapacitor Cells. *Electrochim. Acta* **2016**, *219*, 447−452.
(14) Yang, C. H.; Nguyen, Q. D.; Chen, T. H.; Helal, A. S.; Li, J.; Chang, J. K. Functional Group-Dependent Supercapacitive and Aging Properties of Activated Carbon Electrodes in Organic Electrolyte. *ACS Sustainable Chem. Eng.* **2018**, *6*, 1208−1214.
(15) Hahn, M.; Kotz, R.; Gallay, R.; Siggel, A. Pressure Evolution in Propylene Carbonate Based Electrochemical Double Layer Capacitors. *Electrochim. Acta* **2006**, *52*, 1709−1712.
(16) Jerabek, E. C.; Mansfield, S. F. Methods of Making an Ultracapacitor Electrode. U.S. Patent, US6,084,766, 2000.
(17) Yu, Z.; Tetard, L.; Zhai, L.; Thomas, J. Supercapacitor Electrode Materials: Nanostructures from 0 to 3 Dimensions. *Energy Environ. Sci.* **2015**, *8*, 702−730.
(18) Cazorla-Amorós, D.; Castello, D. L.; Morallon, E.; Martinez, M. J. B.; Solano, A. L.; Shiraishi, S. Measuring Cycle Efficiency and Capacitance of Chemically Activated Carbons in Propylene Carbonate. *Carbon* **2010**, *48*, 1451−1456.
(19) Azaïs, P.; Duclaux, L.; Florian, P.; Massiot, D.; Rodenas, M. A. L.; Solano, A. L.; Peres, J. P.; Jehoulet, C.; Beguin, F. Causes of Supercapacitors Ageing in Organic Electrolyte. *J. Power Sources* **2007**, *171*, 1046−1053.
(20) Deng, Y.; Xie, Y.; Zou, K.; Ji, X. Review on Recent Advances in Nitrogen-Doped Carbons: Preparations and Applications in Supercapacitors. *J. Mater. Chem. A* **2016**, *4*, 1144−1173.
(21) Inagaki, M.; Konno, H.; Tanaike, O. Carbon Materials for Electrochemical Capacitors. *J. Power Sources* **2010**, *195*, 7880−7903.
(22) Paraknowitsch, J. P.; Thomas, A. Doping Carbons Beyond Nitrogen: An Overview of Advanced Heteroatom Doped Carbons with Boron, Sulphur and Phosphorus for Energy Applications. *Energy Environ. Sci.* **2013**, *6*, 2839−2855.
(23) Li, B.; Dai, F.; Xiao, Q.; Yang, L.; Shen, J.; Zhang, C.; Cai, M. Nitrogen-Doped Activated Carbon for a High Energy Hybrid Supercapacitor. *Energy Environ. Sci.* **2016**, *9*, 102−106.
(24) Salinas-Torres, D.; Shiraishi, S.; Morallon, E.; Amoros, D. C. Improvement of Carbon Materials Performance by Nitrogen Functional Groups in Electrochemical Capacitors in Organic Electrolyte at Severe Conditions. *Carbon* **2015**, *82*, 205−213.
(25) Hulicova-Jurcakova, D.; Seredych, M.; Lu, G. Q.; Bandosz, T. J. Combined Effect of Nitrogen- and Oxygen-Containing Functional Groups of Microporous Activated Carbon on its Electrochemical Performance in Supercapacitors. *Adv. Funct. Mater.* **2009**, *19*, 438−447.
(26) Kwon, T.; Nishihara, H.; Itoi, H.; Yang, Q. H.; Kyotani, T. Enhancement Mechanism of Electrochemical Capacitance in Nitrogen-/Boron-doped Carbons with Uniform Straight Nanochannels. *Langmuir* **2009**, *25*, 11961−11968.
(27) Xu, B.; Hou, S.; Cao, G.; Wu, F.; Yang, Y. Sustainable Nitrogen-doped Porous Carbon with High Surface Areas Prepared from Gelatin for Supercapacitors. *J. Mater. Chem.* **2012**, *22*, 19088−19093.
(28) Candelaria, S. L.; Garcia, B. B.; Liu, D.; Cao, G. Nitrogen Modification of Highly Porous Carbon for Improved Supercapacitor Performance. *J. Mater. Chem.* **2012**, *22*, 9884−9889.
(29) Garcia, B. B.; Candelaria, S. L.; Liu, D.; Sepheri, S.; Cruz, J. A.; Cao, G. High Performance High-Purity Sol-Gel Derived Carbon Supercapacitors from Renewable Sources. *Renewable Energy* **2011**, *36*, 1788−1794.
(30) Hulicova, D.; Kodama, M.; Hatori, H. Electrochemical Performance of Nitrogen-Enriched Carbons in Aqueous and Nonaqueous Supercapacitors. *Chem. Mater.* **2006**, *18*, 2318−2326.
(31) Lota, G.; Frackowiak, E. Pseudocapacitance Effects for Enhancement of Capacitor Performance. *Fuel Cells* **2010**, *10*, 848−855.
(32) Frackowiak, E.; Lota, G.; Machnikowski, J.; Vix-Guterl, C.; Beguin, F. Optimisation of Supercapacitors using Carbons with Controlled Nanotexture and Nitrogen Content. *Electrochim. Acta* **2006**, *51*, 2209−2214.
(33) Laheäär, A.; Ouldriane, S. D.; Lust, E.; Beguin, F. Ammonia Treatment of Activated Carbon Powders for Supercapacitor Electrode Application. *J. Electrochem. Soc.* **2014**, *161*, A568−A575.
(34) Jansen, R. J. J.; Bekkum, H. V. XPS on Nitrogen Containing Functional Groups of Activated Carbon. *Carbon* **1995**, *33*, 1021−1027.
(35) Seredych, M.; Jurcakova, D. H.; Lu, G. Q.; Bandosz, T. J. Surface Functional Groups of Carbons and the Effects of their Chemical Character, Density and Accessibility to ions on Electrochemical Performance. *Carbon* **2008**, *46*, 1475−1488.
(36) Wang, Y.; Xuan, H.; Lin, G.; Wang; Chen, F. Z.; Dong, X. A Melamine-Assisted Chemical Blowing Synthesis of N-doped Activated Carbon Sheets for Supercapacitor Application. *J. Power Sources* **2016**, *319*, 262−270.
(37) Shiraishi, S. Heat-treatment and Nitrogen-doping of Activated Carbons for High Voltage Operation of Electric Double Layer Capacitor. *Key Eng. Mater.* **2011**, *497*, 80−86.
(38) Ding, Z.; Trouillet, V.; Dsoke, S. Are Functional Groups Beneficial or Harmful on the Electrochemical Performance of Activated Carbon Electrodes? *J. Electrochem. Soc.* **2019**, *166*, A1004−A1014.
(39) Jorio, A.; Dresselhaus, M. S.; Saito, R.; Dresselhaus, G. F. *Raman Spectroscopy in Graphene Related System*; Wiley-VCH: German, 2011.
(40) Zhou, M.; Pu, F.; Wang, Z.; Guan, S. Nitrogen-Doped Porous Carbons through KOH Activation with Superior Performance in Supercapacitors. *Carbon* **2014**, *68*, 185−194.
(41) Huang, X.; Qian, W.; Xiang, Y. C.; Zhong, J. Z. N-doped Nanoporous Carbons for the Supercapacitor Application by the Template Carbonization of Glucose: The Systematic Comparison of Different Nitridation Agents. *J. Electroanal. Chem.* **2015**, *748*, 23−33.
(42) Luo, W.; Wang, B.; Heron, C. G.; Allen, M. J.; Morre, J.; Maier, C. S.; Stickle, W. F.; Ji, X. Pyrolysis of Cellulose under Ammonia Leads to Nitrogen-Doped Nanoporous Carbon Generated through Methane Formation. *Nano Lett.* **2014**, *14*, 2225−2229.
(43) Lu, Y.; Santino, L. M.; Acharya, S.; Anandarajah, H.; D'Arcy, J. M. Studying Electrical Conductivity using a 3D Printed Four-Point Probe Station. *J. Chem. Educ.* **2017**, *94*, 950−955.
(44) Zhao, L.; He, R.; Rim, K. T.; Schiros, T.; Kim, K. S.; Zhou, H.; Gutiérrez, C.; Chockalingam, S. P.; Arguello, C. J.; Pálová, L.; Nordlund, D.; Hybertsen, M. S.; Reichman, D. R.; Heinz, T. F.; Kim, P.; Pinczuk, A.; Flynn, G. W.; Pasupathy, A. N. Visualizing Individual Nitrogen Dopants in Monolayer Graphene. *Science* **2011**, *333*, 999−1003.
(45) Bonhomme, F.; Lasségues, J. C.; Servant, L. Raman Spectroelectrochemistry of a Carbon Supercapacitor. *J. Electrochem. Soc.* **2001**, *148*, E450−E458.
(46) Lota, G.; Fic, K.; Frackowiak, E. Carbon Nanotubes and their Composites in Electrochemical Applications,. *Energy Environ. Sci.* **2011**, *4*, 1592−1605.
(47) Abouelamaiem, D. I.; López, M. J. M.; He, G.; Patel, D.; Neville, T. P.; Parkin, I. P.; Castelló, D. L.; Morallón, E.; Amorós, D. C.; Jorge, A. B.; Wang, R.; Ji, S.; Titirici, M. M.; Shearing, P. R.; Brett, D. J. L. New Insights into the Electrochemical Behaviour of Porous Carbon Electrodes for Supercapacitors. *J. Energy Storage* **2018**, *19*, 337−347.
(48) Szubzda, B.; Szmaja, A.; Halama, A. Influence of Structure and Wettability of Supercapacitor Electrodes Carbon Materials on their Electrochemical Properties in Water and Organic Solutions. *Electrochim. Acta* **2012**, *86*, 255−259.
(49) Liu, H. J.; Wang, J.; Wang, C. X.; Xia, Y. Y. Ordered Hierarchical Mesoporous/Microporous Carbon Derived from Mesoporous Titanium-Carbide/Carbon Composites and its Electrochemical Performance in Supercapacitor. *Adv. Energy Mater.* **2011**, *1*, 1101−1108.
(50) Nguyen, Q. D.; Patra, J.; Hsieh, C. T.; Li, J.; Dong, Q. F.; Chang, J. K. Supercapacitive Properties of Micropore- and Mesopore Rich Activated Carbon in Ionic-Liquid Electrolytes with Various Constituent Ions. *ChemSusChem* **2019**, *12*, 449−456.

https://dx.doi.org/10.1021/acsami.0c08440
ACS Appl. Mater. Interfaces 2020, 12, 32797−32805

(51) Chen, T. H.; Yang, C. H.; Su, C. Y.; Lee, T. C.; Dong, Q. F.; Chang, J. K. Electrolyte Engineering: Optimizing High-Rate Double Layer Capacitances of Micropore- and Mesopore-Rich Activated Carbon. *ChemSusChem* **2017**, *10*, 3534−3539.
(52) Liu, X.; Wang, Y.; Zhan, L.; Qiao, W.; Liang, X.; Ling, L. Effect of Oxygen-Containing Functional Groups on the Impedance Behavior of Activated Carbon-Based Electric Double-Layer Capacitors. *J. Solid State Electrochem.* **2011**, *15*, 413−419.
(53) Ahuja, P.; Sahu, V.; Ujjain, S. K.; Sharma, R. K.; Singh, G. Performance Evaluation of Asymmetric Supercapacitor based on Cobalt Manganite Modified Graphene Nanoribbons. *Electrochim. Acta* **2014**, *146*, 429−436.
(54) Conway, B. E. *Electrochemical Supercapacitors: Scientific Fundamentals and Technological Applications*, Kluwer Academic/Plenum: New York, London, 1999.
(55) Yoshida, A.; Tanahashi, I.; Nishino, A. Effect of Concentration of Surface Acidic Functional Groups on Electric Double Layer Properties of Activated Carbon Fibers. *Carbon* **1990**, *28*, 611−615.
(56) Kinage, A. K.; Upare, P. P.; Shivarkar, A. B.; Gupte, S. P. Highly Regio-selective Synthesis of *β*-Amino Alcohol by Reaction with Aniline and Propylene Carbonate in Self-Solvent System over Large Pore Zeolite Catalyst. *Green Sustainable Chem.* **2011**, *01*, 76−84.
(57) Ishimoto, S.; Asakawa, Y.; Shinya, M.; Naoi, K. Degradation Responses of Activated-Carbon-Based EDLCs for Higher Voltage Operation and their Factors. *J. Electrochem. Soc.* **2009**, *156*, A563−A571.
(58) Hahn, M.; Wursig, A.; Gallay, R.; Novak, P.; Kotz, R. Gas Evolution in Activated Carbon/propylene Carbonate Based Double-Layer Capacitors. *Electrochem. Commun.* **2005**, *7*, 925−930.
(59) German, R.; Venet, P.; Sari, A.; Briat, O.; Vinassa, J. M. Electrochemical Double Layer Capacitors (supercapacitors) Ageing Impacts and Comparison on Different Impedance Models. *EPE J.* **2014**, *24*, 6−13.
(60) Nanbu, N.; Ebina, T.; Uno, H.; Ishizawa, S.; Sasaki, Y. Physical and Electrochemical Properties of Quaternary Ammonium bis-(oxalato)borates and their Application to Electric Double-Layer Capacitors. *Electrochim. Acta* **2006**, *52*, 1763−1770.
(61) Ebina, T.; Uno, H.; Ishizawa, S.; Nanbu, N.; Sasaki, Y. Use of Tetraethylammonium bis(oxalato)borate as Electrolyte for Electrical Double-Layer Capacitors. *Chem. Lett.* **2005**, *34*, 1014−1015.

https://dx.doi.org/10.1021/acsami.0c08440
ACS Appl. Mater. Interfaces 2020, 12, 32797−32805

Supporting Information

Manipulation of nitrogen-heteroatom configuration for enhanced charge-storage performance and reliability of nanoporous carbon electrodes

Sutarsis Sutarsis, Jagabandhu Patra, Ching-Yuan Su, Ju Li, Dominic Bresser, Stefano Passerini, Jeng-Kuei Chang*

[a] Institute of Materials Science and Engineering, National Central University, 300 Jhong-Da Road, Taoyuan 32001, Taiwan

[b] Hierarchical Green-Energy Materials (Hi-GEM) Research Center, National Cheng Kung University, 1 University Road, Tainan 70101, Taiwan

[c] Department of Materials Science and Engineering, National Chiao Tung University, 1001 University Road, Hsinchu 30010, Taiwan

[d] Department of Mechanical Engineering, National Central University, 300 Jhong-Da Road, Taoyuan 32001, Taiwan

[e] Department of Nuclear Science and Engineering and Department of Materials Science and Engineering, Massachusetts Institute of Technology, 77 Massachusetts Ave, Cambridge, MA 02139, USA

[f] Helmholtz Institute Ulm (HIU), Helmholtzstrasse 11, D-89081 Ulm, Germany

[g] Karlsruhe Institute of Technology (KIT), P.O. Box 3640, 76021 Karlsruhe, Germany

* Correspondence:

jkchang@nctu.edu.tw (Jeng-Kuei Chang), Phone: +886-3-5712121 ext. 55320

Number of pages: 8

Number of figures: 4

Number of tables: 3

Table S1. Ratios of various functional groups for AC-P, AC-MEL, AC-NH_3, AC-NO samples calculated from XPS C 1s spectra.

	Binding energy (eV)	AC-P	AC-MEL	AC-NH_3	AC-NO
C-C	284.6	58.2%	59.1%	59.3%	60.6%
C-H/C-N	285.0	17.5%	21.5%	22.0%	21.3%
C-OH	286.5	14.2%	12.9%	12.2%	12.0%
C=O	287.5	5.1%	3.1%	3.2%	3.0%
COOH	289.0	5.0%	3.4%	3.3%	3.1%

Table S2. Specific capacitances (F g^{-1}) at various rates for AC-P and AC-NO electrodes measured at different voltages in 1 M $TEABF_4$/PC electrolyte.

Current density	AC-P					AC-NO				
(A g^{-1})	2.50 V	2.75 V	3.00 V	3.25 V	3.50 V	2.50 V	2.75 V	3.00 V	3.25 V	3.50 V
0.5	110	110	107	95	90	112	112	112	112	111
0.8	108	107	105	88	84	111	111	110	108	107
1	106	105	102	84	81	109	108	107	106	104
2	101	99	95	73	70	106	105	104	103	99
3	98	96	90	68	64	104	104	103	100	93
5	93	92	83	62	55	99	99	98	95	86
8	87	85	75	55	48	94	93	93	89	77
10	83	81	69	52	45	91	91	90	86	72
12	80	78	65	48	42	88	87	87	83	69
15	75	73	61	43	37	85	85	84	80	64
20	69	68	55	38	32	81	81	81	76	60
$C_{20}/C_{0.5}$ (%)	63	62	51	40	36	72	72	72	68	54

Table S3. Interfacial contact resistance (R_{inter}) and apparent diffusion coefficient (D_a) values of AC-P and AC-NO cells before and after being floated at 2.50 V and 70 °C for 3 days.

	AC-P	Aged AC-P	AC-NO	Aged AC-NO
R_{inter} (Ω)	3.3	29.4	1.6	11.2
D_a ($cm^2\ s^{-1}$)	1.56×10^{-7}	2.27×10^{-8}	7.86×10^{-7}	1.01×10^{-7}

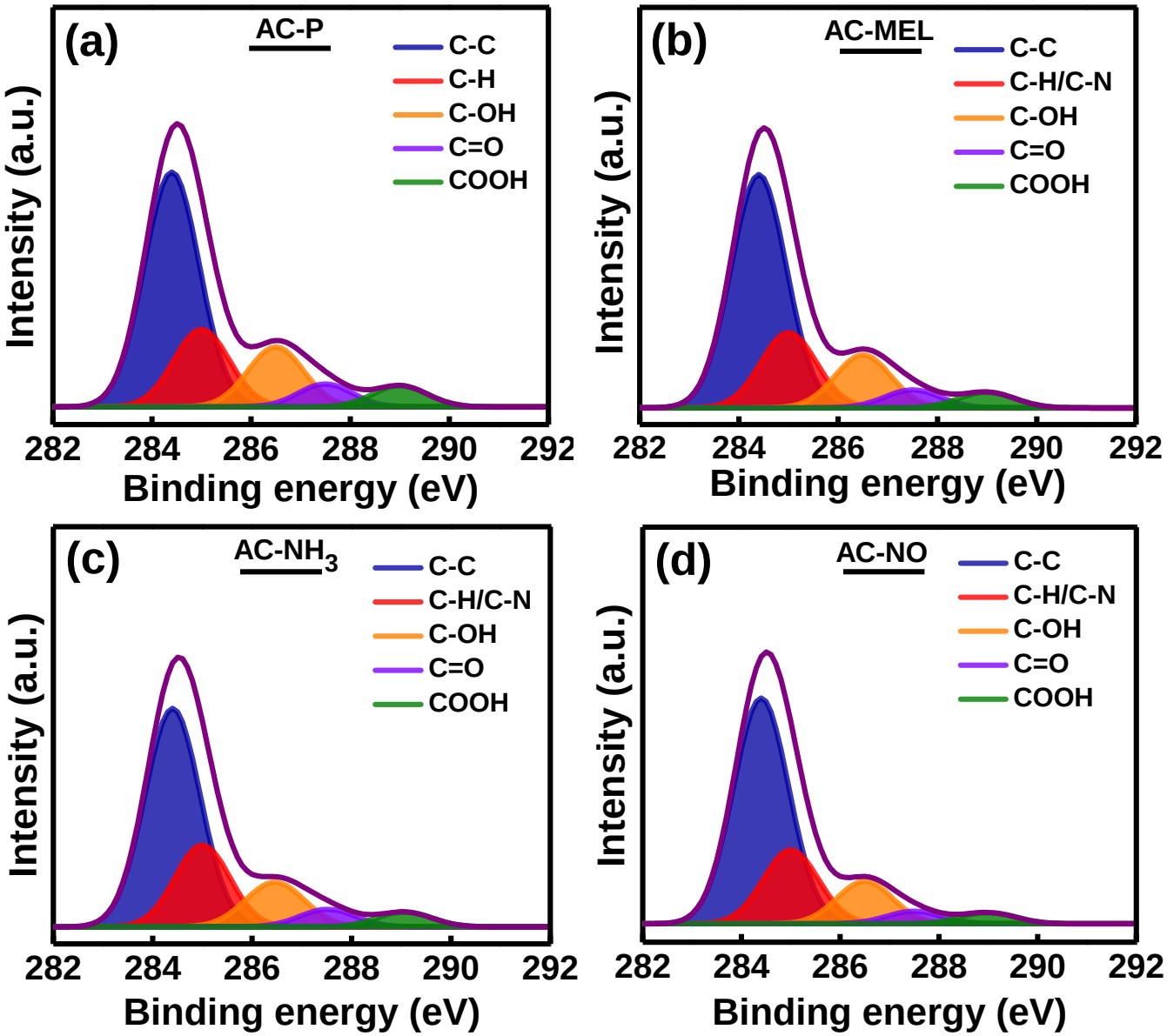

Figure S1. XPS C 1s spectra of (a) AC-P, (b) AC-MEL, (c) AC-NH_3, and (d) AC-NO samples.

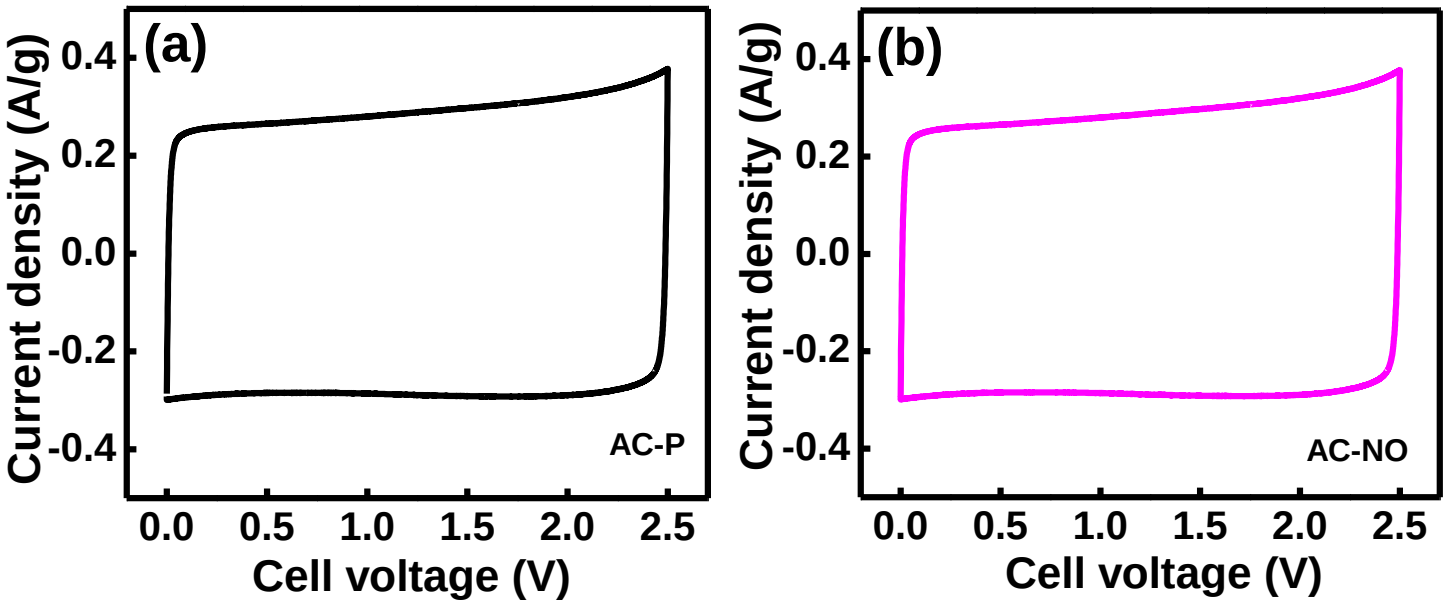

Figure S2. CV curves of (a) AC-P and (b) AC-NO cells measured at 5 mV s^{-1}.

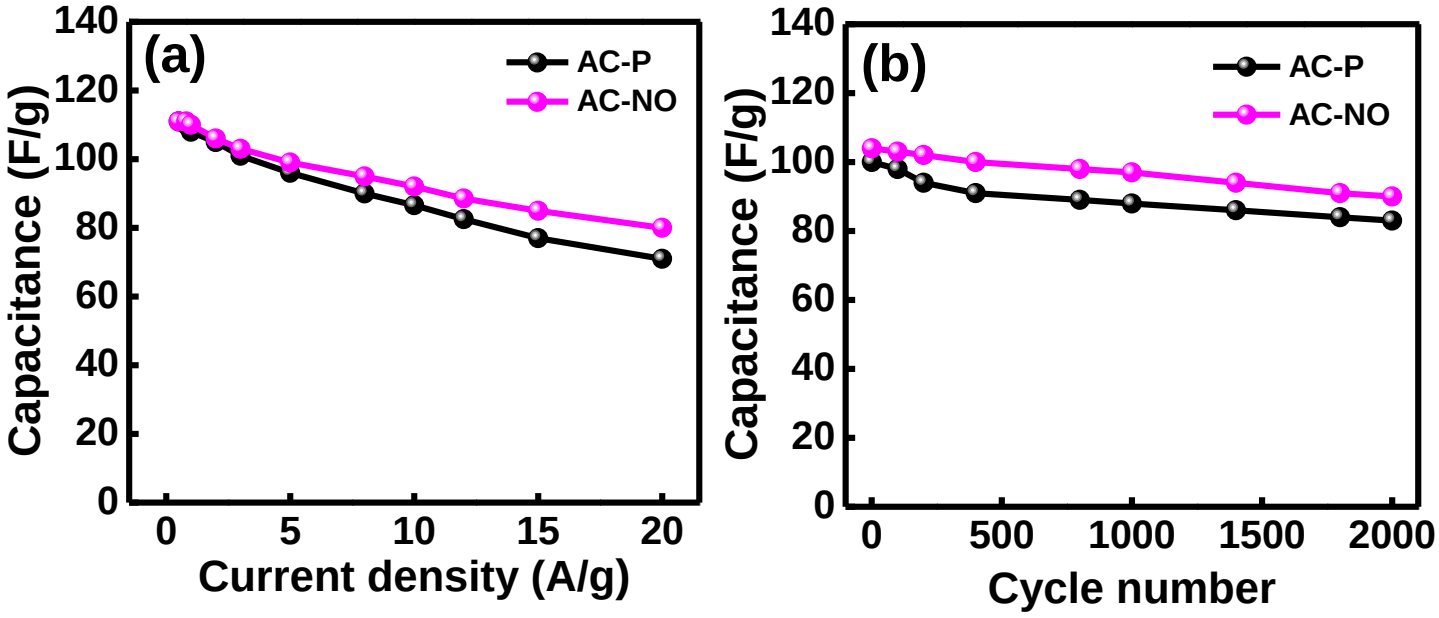

Figure S3. (a) Specific capacitances of AC-P and AC-NO electrodes measured at various rates in 1 M $TEABF_4$/ACN electrolyte. (c) Cycling stability of AC-P and AC-NO cells measured at 5 A g^{-1} in 1 M $TEABF_4$/ACN electrolyte.

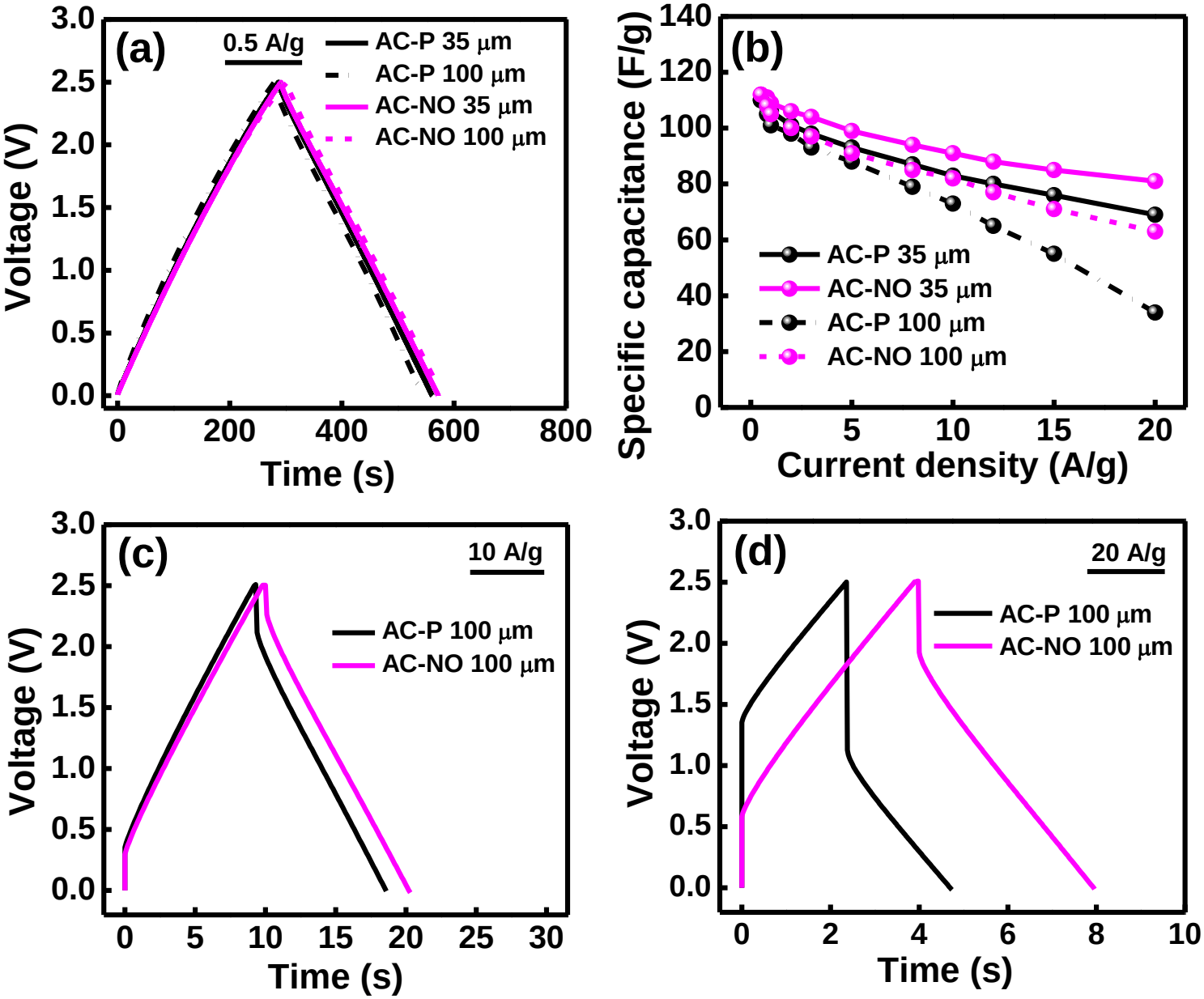

Figure S4. Galvanostatic charge-discharge curves measured at (a) 0.5, (c) 10, and (d) 20 A g^{-1}. (b) Specific capacitances of various electrodes measured at various rates.